

On the effect of cosmic rays in bolometric CMB measurements

S. Masi^{1,2}, E. Battistelli^{1,2}, P. de Bernardis^{1,2}, L. Lamagna^{1,2},
F. Nati^{1,2}, L. Nati^{1,2}, P. Natoli³, G. Polenta^{4,5}, A. Schillaci^{1,2}

¹ Dipartimento di Fisica, Università di Roma “La Sapienza”, Roma, Italy

² INFN Sezione di Roma 1, Roma, Italy

³ Dipartimento di Fisica, Università di “Tor Vergata”, Roma, Italy

⁴ Agenzia Spaziale Italiana - ASI Science Data Center, Frascati, Italy

⁵ INAF - Osservatorio Astronomico di Roma, Monte Porzio Catone, Italy

Submitted: XXX; Accepted: XXX

Abstract. Precision measurements of the anisotropy of the Cosmic Microwave Background (CMB) have the potential to discover low-level non gaussian features due to topological defects or to the inflation process. These measurements are becoming feasible with the development of large arrays of ultra-sensitive bolometric detectors and their use in balloon-borne or satellite missions. However, the space environment includes a population of cosmic rays (CR), which produce spurious spikes in bolometric signals. In this paper we analyze the effect of CR in the measurement of CMB anisotropy maps and in the estimate of cosmological non-gaussianity and of angular power spectra of the CMB. Using accurate simulations of noise and CR events in bolometric detectors, and de-spiking techniques, we produce simulated measured maps and analyze the gaussianity and power spectrum of the maps for different levels and rates of CR events. We find that a de-spiking technique based on outliers removal in the detector signals contributing to the same sky pixel works well in removing CR events larger than the noise. However, low level events hidden in the noise produce a positive shift of the average power signal measured by a bolometer, and increase its variance. If the number of hits per pixel is large enough, the data distribution for each sky pixel is approximately gaussian, but the skewness and the kurtosis of the temperatures of the pixels indicate the presence of low-level non-gaussianity. Moreover, when the low-level CR distribution is not known a-priori, the standard noise estimation pipeline produces a positive bias of the power spectrum at high multipoles. The significance of the bias depends on both the rate of CR events and the time constant and noise properties of the detectors. In the case of a typical balloon-borne survey, the CR-induced non-gaussianity will be marginally detectable in the membrane bolometer channels, while will be negligible in the spider-web bolometer channels. The bias in the power spectra will be avoided using cross-power-spectra from independent channels. In experiments with detector sensitivity better than $100 \mu K / \sqrt{Hz}$, in an environment less favorable than the earth stratosphere, the CR-induced non gaussianity is likely to affect significantly the results.

1. Introduction

Information about the early Universe is encoded in the primary anisotropy of the CMB. While the gaussian fluctuations expected in the adiabatic inflationary scenario beautifully fit the available power spectrum data (see e.g. Nolta et al. 2009), non-gaussian signals are also expected at lower level in the maps, due to non-linearities in the inflation potential (see e.g. Verde et al. 2000) and/or to the presence of topological defects (see e.g. Kaiser & Stebbins 1984). In addition, non-gaussian secondary anisotropies are imprinted in the post-recombination universe, due to the interaction of CMB photons with the large scale structures present in the Universe, and to the emission of Galactic and extra-Galactic sources. The study of primordial non-gaussianity can in principle allow to confirm and select an inflation model, but the signal to be detected is very small. For

this reason it is mandatory to be sure that the measurement system does not introduce non-gaussian features in the data.

Arrays of microwave detectors feature high mapping speed and are now starting to operate at the focus of large telescopes (see e.g. Sayers et al. 2009, Siringo et al. 2009, Carlstrom et al. 2009, Wilson et al. 2008, Swetz et al. 2008) or in CMB polarimeters (see e.g. Hinderks et al. 2009, Yoon et al. 2006, Kuo et al. 2006, Samtleben et al., 2007). TES Bolometric detectors, involving only lithographic fabrication techniques, are easier to replicate in large arrays, and extremely sensitive.

To fully exploit their sensitivity, the radiative background has to be minimized. In this sense, the best solution is to use bolometric detectors in space, possibly feeding them by means of a cryogenic telescope or optical system. The bolometers of the HFI instrument on the Planck mission (Holmes et al. 2008) and those of the PACS and SPIRE instruments on the Herschel

mission (Billot *et al.* 2009, Schultz *et al.* 2008) represent a first step in this direction.

Being extremely sensitive to any form of energy deposited on their absorber and on their thermistors, bolometers are also sensitive to cosmic rays. The energy deposited by a single MeV proton in a cryogenic bolometer is much larger than the typical level of the noise (see e.g. Caserta *et al.* 1990): if an amount of energy ΔE is deposited in a bolometer in a time much shorter than the bolometer time constant, the temperature rise of the bolometer will be $\Delta T = \Delta E/C$ where C is the heat capacity of the detector. This peak level will be achieved in a time shorter than the time constant; the subsequent decay, instead, will be timed by the time constant. The typical noise of a bolometer corresponds to physical temperature fluctuations much lower than $\Delta E/C$, so most CR-induced spikes will be evident in the bolometer time-ordered-data.

To allow the operation of bolometers in unprotected environments (like in sub-orbital or orbital space instruments), special low cross-section bolometers have been developed (spider-webs: Mauskopf *et al.* 1997, wire-grids: Jones *et al.* 2003). An additional benefit of these low-cross-section detectors is the reduced heat capacity with respect to solid-absorber or membrane-absorber ones, resulting in a shorter time constant.

In a polar stratospheric balloon flight the rate of cosmic rays events in low cross-section (spider-web) bolometers cooled at 0.3K is of the order of 0.1 Hz (Masi *et al.* 2006), which is about 20 times less than the rate of events for solid/membrane-absorber bolometers at the same temperature in the same environment. The events are produced either by primary CR interacting directly with the detectors, or by secondary particles, including showers of electrons and bremsstrahlung-produced gammas, resulting from the interactions of primary cosmic rays in the metal surrounding the bolometric detector. Lower temperature detectors feature lower noise with basically the same geometry, so that the rate of CR events above the noise level will be even higher; this effect is in part mitigated by their faster response.

Balloon-borne missions, using bolometer arrays, currently under development, include among others the EBEX CMB polarimeter (Oxley *et al.* 2004), the SPIDER experiment to detect CMB polarization at larger angular scales (Crill *et al.*, 2008), the OLIMPO telescope, mainly devoted to high frequency observations of the Sunyaev-Zeldovich effect (Nati *et al.*, 2007), the BLAST/BLASTPOL telescope devoted to far infrared cosmological and galactic studies (Pascale *et al.*, 2008, Marsden *et al.*, 2008). Given the fast mapping speed of large arrays of bolometers and the fast and relatively cheap access to space provided by stratospheric balloons, we expect these efforts to continue in the future. It is thus relevant to focus on the stratospheric case.

The data from a bolometric detector can be cleaned by detecting the spikes and flagging the corresponding section of data as not usable for further analysis. For filtering purposes the masked data can be filled with constrained realizations of noise with the same properties as the surrounding data (see e.g. Masi *et al.* 2006). However, in the absence of independent cosmic rays monitors, a number of low level events will remain unidentified, hidden in the noise. If the bolometer is non-ideal,

and features an additional long time constant, the effect of CR can be an increase of 1/f noise. In this paper we focus on the undetected cosmic rays hits and study how they can affect the analysis of data aimed at measuring CMB anisotropy and non-gaussianity.

2. Simulation of bolometer time-ordered data

In order to study the effect of CR events, we simulated first time-streams of bolometer data in the absence of sky signals, i.e. we just added CR events to a gaussian realization of noise $G(t)$ with a given standard deviation σ and null average. The time-ordered samples of bolometer noise are built as a gaussian realization, filtered with a first order low pass filter simulating the thermal response of the detector.

We have considered three reference cases with different bolometer time constants and CR rates: case R_1 has a rate of 2 Hz for a slow, membrane absorber bolometer at 0.3K ($\tau = 70ms$), case R_2 has the same rate for a faster membrane-absorber bolometer at 0.1K ($\tau = 10ms$), case R_3 is a low-cross section bolometer (spider-web) with a rate of 0.1 Hz and a time constant $\tau = 10ms$.

The waiting times for CR events follow an exponential distribution with a rate R :

$$P(t) = R e^{-Rt}, t > 0. \quad (1)$$

The amplitudes A of the pulses induced by CR are assumed to follow an exponential distribution with average $\langle A \rangle$. The exact shape of such a distribution for a given experiment will depend on the spectra of primary cosmic rays in the environment of operation, on the distribution and characteristics of the material surrounding the bolometer, on the shape of the sensitive element of the bolometer itself, and on the angular distribution of the incoming cosmic rays in the restframe of the bolometer sensor. The important parameter, however, is the fraction of events with amplitude lower than say 3σ : these are likely to remain hidden in the noise. In the case of the exponential distribution we have selected, this fraction is $1 - \exp(-3\sigma/\langle A \rangle)$. This is $\sim 26\%$ if $\langle A \rangle/\sigma = 10$.

The shape of each pulse is modeled as a sudden level jump of amplitude A , followed by an exponential decay with time constant τ :

$$D(t) = A e^{-t/\tau}. \quad (2)$$

For 10 time constants after the CR event the simulated data are obtained as $S(t) = D(t) + G(t)$; elsewhere the simulated data are simply $G(t)$: for our starting tests, we do not include sky signals in the simulation.

In fig. 1, 2 and 3 we show sample subsections of simulated data. Large CR spikes are evident, but smaller ones remain hidden in the noise.

3. Despiking the time-ordered data

Evident CR events (with amplitude larger than say 4σ) can be easily identified and removed. In order to remove smaller CR spikes, one can take advantage of the peculiar shape of these

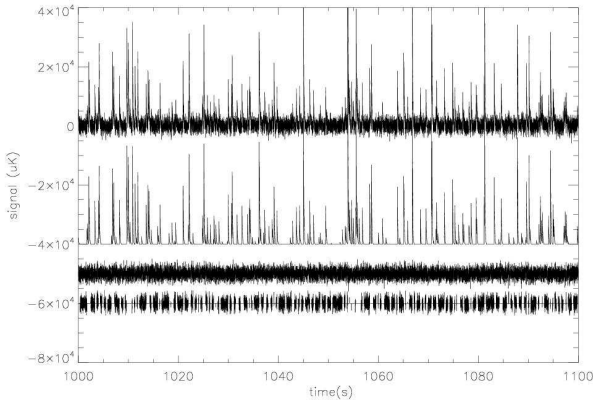


Fig. 1. Top line: sample subsection of simulated bolometer data $S(t)$ (converted in μK_{CMB}) resulting from the sum of spikes from CR events $D(t)$ (middle top line, offset -40 mK for clarity of visualization) and bolometer noise $G(t)$ (middle bottom line, offset -50 mK). In this simulation the signal is sampled at 200Hz, $\sigma = 1.4$ mK, $\tau = 0.07$ s, $R = 2.0$ Hz and $\langle A \rangle = 10$ mK (case R_1). Comparing the top and middle lines it is evident that many CR events remain hidden in the noise and are very difficult to identify. In the bottom line (offset -60 mK) we plot the data de-spiked following the pixel-based procedure described in the text. The missing data have been flagged as not usable since they are within 5 time constants of a detected spike.

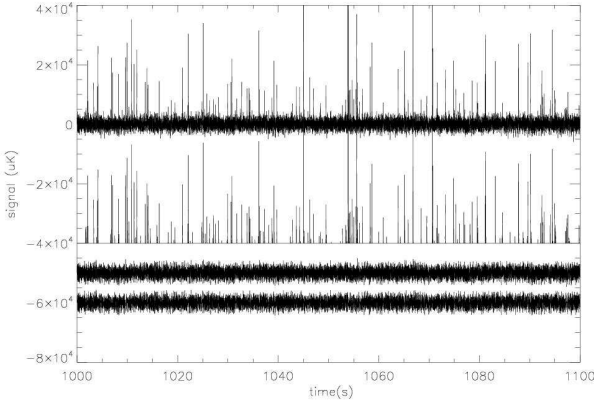


Fig. 2. Same as fig. 1, with $\tau = 0.01$ s, $R = 2.0$ Hz and $\langle A \rangle = 10$ mK (case R_2). Comparing the top and the middle lines it is evident that many CR events remain hidden in the noise and are very difficult to identify.

signals. The exact shape depends on the bolometer configuration (single or double time constant, or even more complex response) and on the details of the front-end electronics, amplifying the nV-level bolometer signals. In our simulations we have used a simple exponential decay, but it is not difficult to extend our analysis to more complex shapes, once the impulsive response of the system is known from calibrations.

A standard method to identify events embedded in noise is to look for correlations between the noisy time ordered data

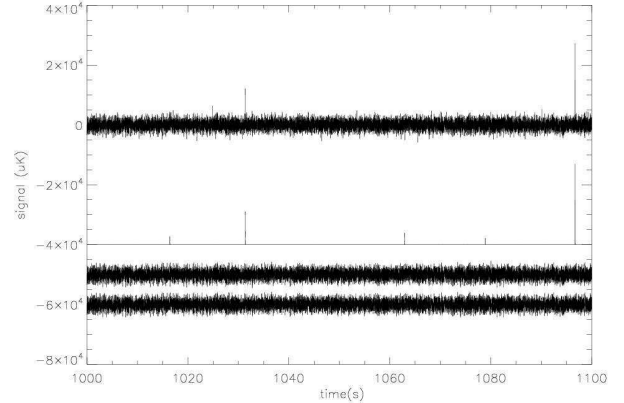


Fig. 3. Same as fig. 1, with $\tau = 0.01$ s, $R = 0.1$ Hz and $\langle A \rangle = 10$ mK (case R_3). Comparing the top and the middle lines it is evident that some CR events can remain hidden in the noise.

and an event template. As an estimator of the correlation we have computed the normalized convolution

$$C(t) = \frac{\int_0^{10\tau} S(t+u)D(u)du}{\int_0^{10\tau} D(u)du} \quad (3)$$

In the absence of noise this correlation is positive for all times t where a CR event is contaminating the signal. The presence of noise induces fluctuations in $C(t)$ which, however, are smaller than the fluctuations in $S(t)$, so there is a gain in using this estimator. We can set a positive threshold T and assume that all the samples with $C(t) > T$ are contaminated by CR events. To analyze the efficiency and accuracy of this CR detection method, we have considered the contaminated samples as a function of the threshold level T , and computed the fractions f_i and f_f . f_i is the fraction of events which have $C(t) > T$ and $D(t) > D_{min}$, where $D_{min} = 1\mu K$: these are true detections of CR events. f_f is the fraction of samples where $C(t) > T$ while $D(t) < D_{min}$: these are false detections due to the noise mimicking CR events. For an average amplitude of the CR events equal to 7 times the rms of the noise ($\langle A \rangle = 10\sigma$), 50% (0.4%) of the samples are contaminated for case R_1 (R_3).

We find that, due to the noise, the convolution-based method fails to identify a number of contaminated samples, and introduces a large number of false detections. In particular, for R_1 we get $f_i = (37, 27, 16)\%$ and $f_f = (2.9, 0.3, 0.005)\%$ for $T = (0.5, 1, 2)\sigma$. In other words, in order to avoid a large number of false detections, one is forced to raise the threshold level, but then many CR events are missed. For R_3 we get $f_i = (33, 24, 13)\%$ and $f_f = (19, 3.8, 0.02)\%$ for $T = (0.5, 1, 2)\sigma$, confirming the inefficiency of the method. The situation is even worse if the ratio $\langle A \rangle / \sigma$ is reduced.

4. Pixel-space despiking

In addition to the problems listed in the previous section, removing CR pulses directly from the time-ordered data is dangerous, because of the risk of removing real sky signals (for example fast signals produced by scans over point sources).

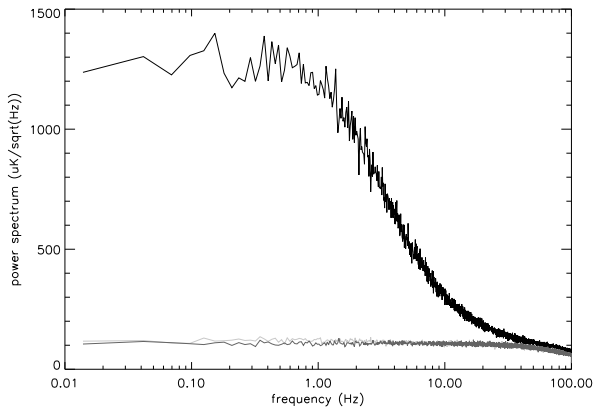


Fig. 4. Power spectrum of the data for case R_1 (top line), of the despiked data (middle line) and of the original noise-only data (bottom line). The despiking procedure does not introduce spectral features in the data.

A better strategy is to analyze the set of data samples contributing to the same sky pixel: for all those samples the sky signal is the same, so outliers must be due either to detector noise or to CR events. We use a simple iterative procedure to remove outliers. For a given pixel p the average $\langle S \rangle_p$ and the standard deviation σ_p of all the contributing signals S_k are computed. If for sample k the difference $S_k - \langle S \rangle_p$ is larger than $3\sigma_p$, the sample is classified as an outlier, and removed. A new average and a new variance are computed from the remaining samples of the set, and new outliers are identified and removed. This procedure is repeated until the average and the variance do not change anymore (no or very few new outliers are found).

In general, only a few iterations are needed to achieve convergence. We find that after 6 iterations the efficiency of this removal method is similar to that of the convolution-based one, but with this method we do not risk to cut real sky signals.

The despiked timelines are very similar to the noise-only time-lines, and their spectrum (vs. frequency) closely resembles the noise spectrum, as shown in fig. 4 for our worst-case R_1 .

The average in each pixel converges to a positive value, while from detector noise only it would be very close to zero. This is due to the effect of CR hits with amplitude smaller than the noise: these remain undetected and produce a positive bias. Also, they increase the standard deviation of the data contributing to the same pixel.

For this reason the 1-point distribution of temperatures in pixels obtained after the averaging and the outliers-removal processes will be shifted towards positive values, and broader than expected from instrument noise only.

The data after a CR event are contaminated for a certain amount of time, depending on the spike amplitude and on the time constants of the system. Some of these data might be recovered removing a best-fit spike profile from the timeline. However, due to the effect of noise, the fit will not be perfect. We prefer to be conservative, and just flag as not usable all the data after a spike, for a period of 5 time constants. The fraction

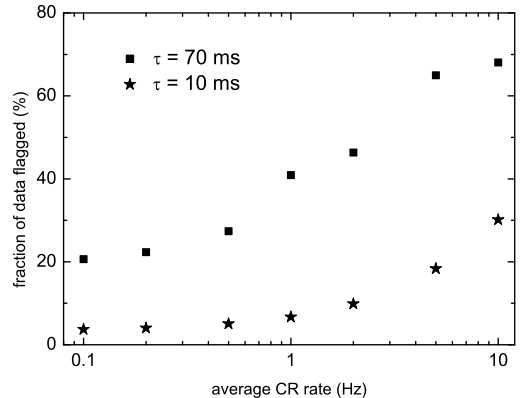


Fig. 5. Fraction of data flagged as contaminated by CR events, vs average CR rate, in a bolometric experiment. A detector noise of $100 \mu\text{K}/\sqrt{\text{Hz}}$ and an average amplitude of CR events of 10 mK have been assumed. Squares refer to fast detectors (time constant of 10 ms), stars refer to slow detectors (time constant of 70 ms). A pixel-based de-spiking algorithm iteratively clipping all the data at more than 3σ from the pixel average has been used. All data within 5 time constants of a CR event have been flagged.

of flagged data is plotted in fig. 5 for different CR rates and bolometer time constants.

In the following we study two different cases. The first one is a targeted observation of a small map (about $1.5^\circ \times 1.5^\circ$ in size, with a $4'$ FWHM resolution) for a relatively short time (10 hours of integration for a single detector), like the maps observed by the OLIMPO experiment to measure the Sunyaev-Zeldovich effect in well known clusters (Nati *et al.* 2007). The second one is the observation of a large (about $10^\circ \times 10^\circ$ in size) deep survey of a clean region, with 7 days of integration. This is similar to the blind deep survey of CMB and undetected SZ clusters carried out by OLIMPO. We assume the same angular resolution for this survey as well.

In fig. 6, 7 and 8 we plot the 1-point distributions vs. the iteration number in the case of observations of 4320 independent pixels (small map case), in our three reference cases, for a total integration time on the map of 10 hours.

The results for the moments of these distributions are reported in table 1.

It is clear that the outliers removal process works, since the 1-point distribution approaches a gaussian distribution after a few iterations. The skewness and kurtosis of the 1-point distribution go back to values consistent with zero, after the despiking process. This means that the number of low level spikes averaged in each pixel is large enough to gaussianize the result, at least at the level of sensitivity considered here.

However, the positive bias and the increase of the variance in the estimated pixel temperatures due to undetected CR are still present, as evident from fig. 6 and 7 and table 1.

If the average rate of CR hits is not constant during the observations of different pixels, this positive bias will vary ac-

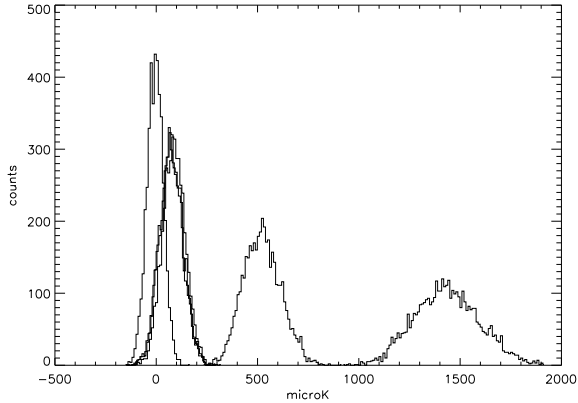


Fig. 6. 1-point distributions of pixel temperatures estimates $\langle S \rangle_p$ vs despiking iteration. In this simulation there is no sky signal, the detector NET is $100 \mu K \sqrt{s}$, the time constant is 70 ms, the sampling rate is 200 Hz ($\sigma = 1.4 mK$) the total integration time for 4320 pixels is 10 hours, in an environment producing an average amplitude of CR events of 10 mK and an average rate of 2 Hz (case R_1). The rightmost distribution is what one would measure by averaging the data in pixels without any despiking. After each outliers removal iteration, the 1-point distribution moves to the left, approaching a gaussian distribution but remaining shifted with respect to the distribution of detector noise without CR events (which is the leftmost histogram).

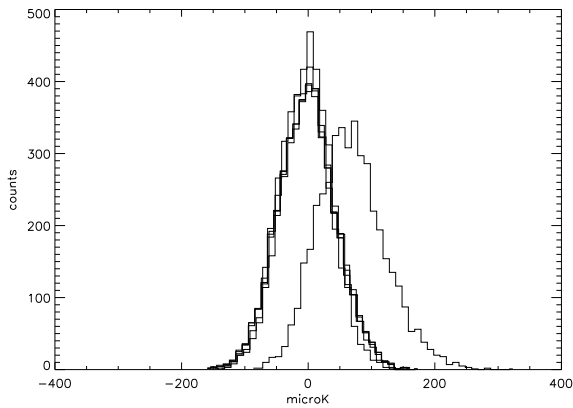


Fig. 7. Same as fig. 6 with a time constant of 10 ms, in an environment producing an average amplitude of CR events of 10 mK and an average rate of 2.0 Hz (case R_2).

cordingly, introducing fake structures in the measured maps. A modulation of the CR rate can be introduced by the scanning strategy of the instrument, which induces variations in the absorbing material in-between the CR flux and the bolometers, thus producing scan-synchronous systematic effects. For example an asymmetric satellite spinning in the solar wind could introduce spurious dipole or higher order anisotropy (depending on the actual structure of the satellite) aligned to the solar wind direction. It would be very useful to include in the instrumental setup an independent CR flux monitor, as close as possible to the focal plane bolometers. The level of the spurious signal de-

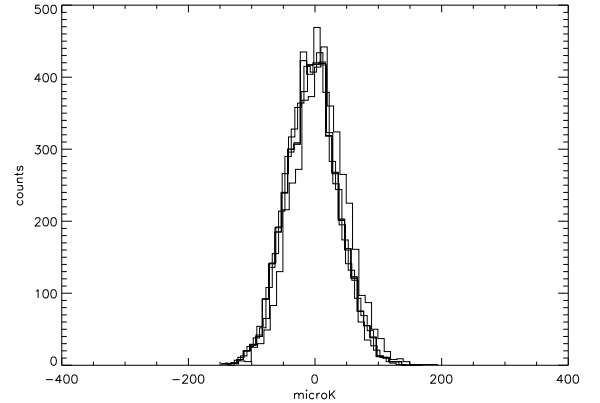


Fig. 8. Same as fig. 6 with a time constant of 10 ms, in an environment producing an average amplitude of CR events of 10 mK and an average rate of 0.1 Hz (case R_3).

pends on the CR composition, flux and spectrum, on the cross-section of the bolometers, on the structure of the instrument; this can be quantified only focusing on the specific case.

Even if the CR flux is perfectly steady, the increase of the variance of the detected data for each pixel can bias the noise estimates which are needed to estimate the power spectra. In fact, in the standard analysis procedure for CMB maps one estimates the noise from the data, assuming gaussian noise, and then uses gaussian monte-carlo simulations to assess the bias on the power spectrum (see e.g. Hivon et al. 2002, Polenta et al. 2005).

In principle this fact can bias the noise estimates, and, at lower level, might affect the non-gaussianity parameters relevant for cosmology.

These effects are studied in the following paragraphs, where we focus on observations of the larger survey, which is most useful to beat cosmic variance and measure the power spectrum of the CMB and non-gaussianity parameters. This ~ 100 square degrees map contains $N = 86070$ $1.7'$ pixels. A total integration time of 1 week has been assumed.

We define a data timeline contaminated by spikes for the cases R_1 and R_3 described above (70 and 10 ms detector time constant, respectively). These are, respectively, the hardest and mildest case considered in this paper, from the point of view of CR contamination.

We thus perform iterative despiking as described above, and analyze the resulting large maps.

5. Tests of Gaussianity

Primordial CMB anisotropies are known to be Gaussian distributed to leading order (see e.g. Komatsu et al. 2003, De Troia et al., 2003 Natoli et al., 2009). Small deviations from Gaussianity have however been predicted and, if observed, may be used to constrain inflationary models (see Bartolo et al. 2004 for a review).

Measures of this non Gaussian component are however hampered by several sources of instrumental or non instrumen-

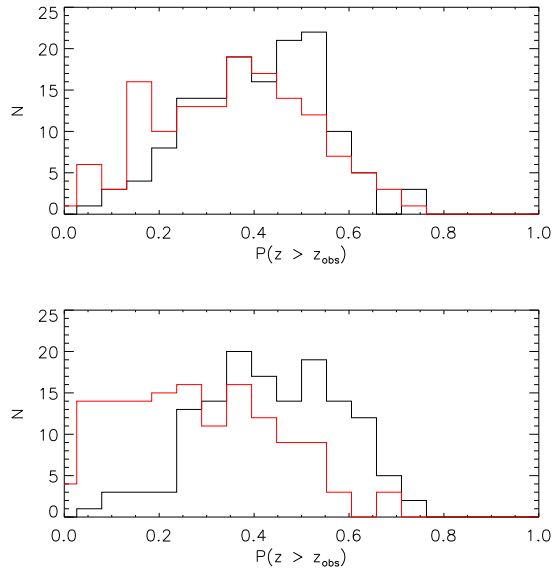


Fig. 9. Histogrammed probabilities for the KS test, for the R_1 and R_3 (bottom) cases.

tal (e.g., foreground contamination) systematic effects, which may induce spurious non Gaussian signatures in the data.

In particular, undetected cosmic ray hits add a non Gaussian contribution to detector noise, which is usually assumed to be normally distributed otherwise. Furthermore, the despiking procedures described above are based on clipping and may also alter the statistics of the dataset.

We first perform a Kolmogorov-Smirnov (KS) test on the pixel values for (1) five iteration despiking for the R_1 and R_3 and (2) no CR contamination, the latter to be used as the reference purely Gaussian dataset. The KS test (see Press et al. 1992) is a standard test to quantify the probability whether a sample can be ascribed to a given distribution. It can also be used to reject the null hypothesis that two different samples are drawn from the same distribution. For each map we compute the KS measure:

$$D_{\text{obs}} = \max_t |S_N(t) - F(t)|$$

where t is the map temperature value, F the cumulative of the Gaussian distribution function and S_N the empirical distribution function of a simulated noise map. We also define $Z_{\text{obs}} = D_{\text{obs}} \sqrt{N}$. The KS test provides a probability $P(Z > Z_{\text{obs}})$ for a given map. We plot in Fig. 9 the KS probabilities obtained for the 140 Monte Carlo map as histograms for the R_1 (left) and R_3 cases, along with their respective Gaussian (no CR) reference set. The R_1 case exhibits clear deviation from its reference Gaussian counterpart, while in the case of R_3 this deviation is not at all evident. Even for R_1 , any single map has (roughly) a 50% probability to be flagged as non Gaussian by our KS analysis. The same considerations apply to the observed distribution of the Z coefficients, shown in Fig 10.

To further quantify our detection of non Gaussianity, we define two simple NG estimators as the normalized skewness (S_3) and kurtosis (S_4) of each map. The corresponding his-

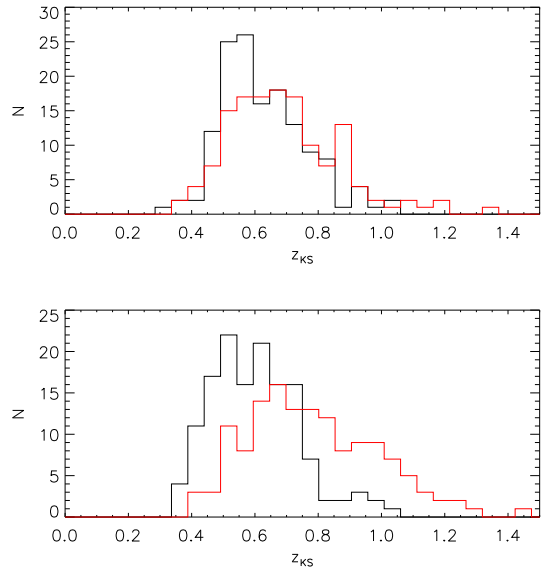


Fig. 10. Same as Fig. 9 but for the Z_{obs} KS coefficients.

tograms are shown in Fig. 11, again for the cases R_1 , R_3 and their respective reference Gaussian sets. Note here how the R_3 case also exhibits deviation from Gaussianity in the case of the kurtosis. The empirical (histogrammed) distribution function can themselves be subject to a KS test against their Gaussian reference sets: in this case one simply measures the distance between the empirical cumulative distribution functions. This test rejects at high significance ($> 99.99\%$) the null hypothesis that the distribution of S_3 and S_4 is Gaussian for the R_1 case. For R_3 , the Gaussianity of S_4 is also rejected with similar confidence, but the null hypothesis is accepted ($P > 35\%$) for the S_3 case.

In conclusion, the non Gaussianity level induced by CR contamination in the large noise maps is weak and cannot be detected with high statistical significance even in the R_1 case, while the R_3 maps are, taken one at a time, indistinguishable from Gaussian maps, at least for the tests employed here. However, the situation changes when a *set* of maps is considered: our Monte Carlo analysis shows that, when a moderate number (140 in our case) are analyzed jointly, non Gaussian signatures are detected even for R_3 . As a consequence, an experiment that uses a similar kind of detectors but gathers significantly more data than considered here, may be prone to CR-induced non Gaussianity, especially when high precision measurements are sought after.

6. Biasing of power spectra

The angular power spectrum of the CMB is a most valuable cosmological observable, which can be used to extract information about the underlying physical model. Thus, it is critical to assess the effect of contamination from residual, undetected spikes.

We thus estimate the angular power spectrum using cROMASTER, a pseudo- C_ℓ estimator based on MASTER (Hivon et al. 2002), originally developed for (and applied to)

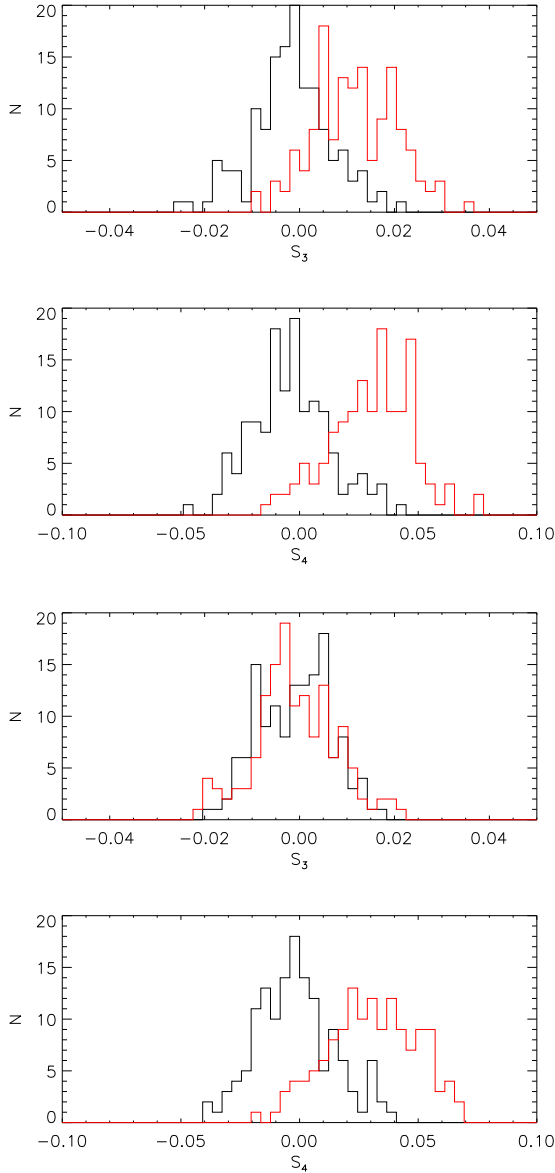


Fig. 11. Empirical observed probabilities for skewness (S_3) and kurtosis (S_4), sampled from 140 Monte Carlo noise maps. Shown are again the R_1 (top) and R_3 cases.

BOOMERanG-B03 (Jones et al. 2006, Piacentini et al. 2006, Montroy et al. 2006, Masi et al. 2006) and later improved for PLANCK data analysis. cROMASter can estimate both auto- and cross-power spectra, where the former are more efficient but require noise removal and the latter are less efficient but are naturally unbiased (Polenta et al. 2005), therefore residual bias is not expected in the pure cross-spectrum case. We have verified this assertion through simulations. The case of auto-spectra is more delicate since they require a companion monte-carlo dataset to estimate and remove residual noise.

In order to verify the effect of the spikes we have firstly generated a monte-carlo dataset that ignores the presence of residual spikes themselves, and only relies on the nominal detector

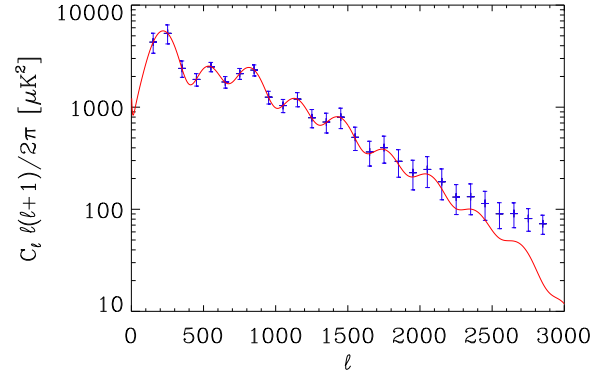


Fig. 12. Simulated measurement of the power spectrum of CMB anisotropy in a bolometric experiment affected by CR hits as in case R_1 . The noise estimate has neglected the presence of CR spikes. As a result, the spectrum is heavily biased.

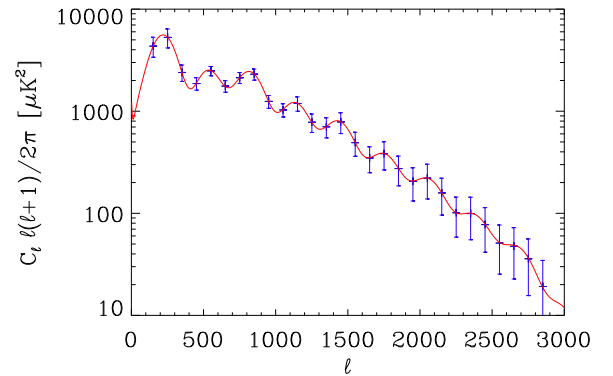


Fig. 13. Same as fig. 12. Here the noise estimate has included the presence of CR spikes, assuming that their distribution is known a-priori. As a result, the spectrum is not biased.

noise level. When using this dataset as noise estimate the resulting power spectrum is heavily biased, as shown in fig. 12.

Thus taking into account the effect of spikes in the monte-carlo dataset is important. This can be done in two ways: the first and in principle more precise is to process the monte-carlo timelines by adding simulated spike signal with the same properties of the spikes seen in real data. When this is performed a bias free auto-spectrum can be obtained as shown in fig. 13.

However, this procedure relies on the knowledge of the underlying spike's rate and distribution. The spike characteristics and statistics can in principle be extrapolated from the data themselves, relying on the observed events. Such a procedure, however, complicates significantly the noise estimation and monte-carlo generation pipeline of the experiment. Moreover, this approach is prone to biases, since the estimated statistics are derived from the most energetic CR events, which are detected above the noise, while the low energy ones, which contaminate the data, are not detected: their distribution can only

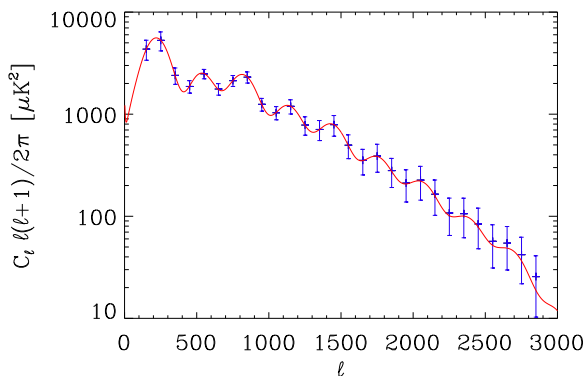


Fig. 14. Same as fig. 12. Here the noise estimate has been performed from the dataset using a standard pipeline, i.e. subtracting the best fit signal contribution from the data timelines. The non-gaussian nature of the residual spikes has been neglected. The residual bias in the power spectrum is small, and appears to be limited to the highest multipoles.

be estimated by means of analytic extrapolations of the high energy distribution. The reliability is thus completely unknown.

We have thus verified if a simpler approach would produce results accurate enough for power spectrum estimation. For this second scheme we estimate the noise properties from the data that are contaminated by spikes but, when turning to timeline simulation, we avoid modelling the spike contribution and despiking procedure. In practice we first measure the noise properties of the despiked timeline, after subtracting the signal contribution by means of standard iterative techniques (Ferreira and Jaffe 2000), and use this dataset to estimate the noise power spectrum. Since a timeline contaminated by spikes exhibits some level of non Gaussianity, the noise power spectrum does not encode all the information about our noise properties. However, we ignore this complication, and use the estimated spectrum information to generate stationary Gaussian realization of noise. Since the spike residual is likely non-Gaussian, this procedure is not strictly correct. However, as shown in fig. 14, the residual bias we obtain is -visually- very small.

To quantify this statement, we have performed the Hausman test (Polenta et al. 2005) on the band power we obtain from our simulations. The Hausman test is a powerful procedure to assess the significance of a residual noise bias in the spectrum. It makes use of both cross spectra and auto spectra estimates. We restrict ourselves to the R_1 and R_3 cases described above. We define three test statistics to detect a bias in the noise estimation: $s_1 = \sup_r B_L(r)$, $s_2 = \sup_r |B_L(r)|$ and $s_3 = \int_0^1 B_L^2(r) dr$, where $B_L(r)$ is the random process defined in Polenta et al. 2005 from the measured power spectrum. We use monte-carlo simulations to draw their empirical distributions. Our results for the confidence of bias detection with 68%, 95% and 99% probability are shown in Table 2.

It can be noticed that, despite being small, the bias can be always detected at high statistical significance. This is a strong indication that the noise estimation pipeline for an high precision experiment must account for the presence of spikes in a

	68%	95%	99%
s_1	100%	96 %	87%
s_2	99 %	93%	70%
s_3	96%	69%	39%
s_1	59 %	19 %	10 %
s_2	48 %	15 %	7 %
s_3	38 %	8%	1.4%

Table 2. Confidence level for bias detection with the Hausman test in cases R_1 (top three lines) and R_3 (bottom three lines), with a naively simulated noise estimation pipeline (see text). s_1 , s_2 and s_3 are three different bias estimators defined in Polenta et al. 2005 (see text).

more accurate way than the simple procedure set forth above, at least if auto spectra are desired.

While we do not explicitly simulate here an experiment capable of measuring polarization spectra, it is clear that the same conclusions hold, *a fortiori*, when linear polarization can be measured. On the other hand, a spectral pipeline that only relies on cross spectra is very robust to the effect of spikes.

Hence, cross spectra, while less efficient than autospectra, are certainly more adapt for an experiment contaminated by cosmic rays, at least as long as correlated events between different detectors are excluded.

7. Conclusions

Bolometric observations carried out from space are affected by cosmic rays. The data must be despiked to be used efficiently and to avoid serious biases in the results. Pixel-based outliers removal works well: the power spectra of the despiked timelines closely resemble the original gaussian noise used in the simulation. However, low-level events remain hidden in the noise, resulting in a positive shift of the average signal measured in each pixel, and increasing its variance.

The maps resulting from despiked data are non gaussian. The level of non gaussianity depends on the rate of the spikes, on the deposited energy and on the time constant and noise of the detectors. Using the Skewness and the Kurtosis of the pixel temperatures as simple non-gaussianity indicators, we find that, in the case of the 100 square degrees survey, the CR-induced non-gaussianity is not likely to be detected if spider-web bolometers are used, while would be marginally detectable for slow membrane detectors. For experiments featuring longer integration times and/or lower noise detectors, the CR-induced non-gaussianity will be significant.

Using the standard analysis pipeline on the map estimated from the despiked timeline, the residual hidden events produce a positive bias of the angular power spectrum of the map at high multipoles. In the specific example of the 100 square degrees survey, the expected bias is negligible for spider-web bolometers, while could be important for slow membrane detectors. However, since all the new experiments use bolometer arrays, cross-spectra can be computed in place of auto-spectra. These are virtually insensitive to the CR-induced bias problem. The

only unavoidable problem will be a significant reduction of the effective integration time, in the case of slow membrane detectors.

Acknowledgements. This work has been supported by Italian Space Agency contracts “COFIS” and “OLIMPO” and by PRIN 2006 “Cosmologia Millimetrica con Grandi Mosaici di Rivelatori” of the Ministero dell’Istruzione, dell’Università e della Ricerca.

References

- Bartolo, N., Komatsu, E., Matarrese, S., & Riotto, A. 2004, *Phys. Rep.*, 402, 103
- Billot N., et al., *Astrophysics Detector Workshop 2008* P. Kern (ed) EAS Publications Series, 37 (2009) 119-125
- Carlstrom J.E. et al., 2009, submitted to *PASP*, astro-ph/0907.4445v
- A. Caserta, P. de Bernardis, S. Masi, M. Mattioli, *NUCLEAR INSTRUMENTATION AND METHODS IN PHYSICS RESEARCH A*294, 328-334 (1990)
- Crill B., et al., *Proceedings of SPIE Volume 7010, "Space Telescopes and Instrumentation 2008: Optical, Infrared, and Millimeter"*, Editors: Jacobus M. Oschmann, Jr.; Mattheus W. M. de Graauw; Howard A. MacEwen, arXiv:0807.1548
- De Troia, G., et al., 2003, *MNRAS*, 343, 284-292
- Ferreira, P. G., & Jaffe, A. H. 2000, *MNRAS*, 312, 89
- Hinderks J.R., et al., 2009, *ApJ*, 692, 1221-1246
- Hivon, E., et al., 2002, *ApJ*, 567, 2-17
- Holmes, W. A., et al., *Appl. Opt.* 47, 5996-6008 (2008)
- Jones, W.C., Bhatia, R.S., Bock, J.J., Lange, A.E., 2003, *SPIE*, 4855, 227, astro-ph/0209132
- Jones, W.C., et al., 2006, *ApJ*, 647, 823-832
- Kaiser N. & Stebbins A., 1984, *Nature*, 310, 391.
- Kuo C.L., 2006, *Nuclear Instruments and Methods in Physics Research A*, 559, 608-610
- Komatsu, E., et al., 2003, *ApJS*, 148, 119
- Marsden G., et al., 2008, *SPIE Conference Proceedings*, arXiv:0805.4420
- Masi, S., et al., 2006, *Astronomy and Astrophysics*, 458, 687-716, astro-ph/0507509
- Mauskopf, P.D., Bock, J.J., Del Castillo, H., Holzapfel, W.L., Lange, A.E. 1997, *Applied Optics*, 36, 4
- Montroy T.E., et al., 2006, *ApJ*, 647, 813-822
- Nati, F., et al., *New Astronomy Reviews*, 51 (2007) 385-389
- Natoli, P., et al., 2009, submitted to *MNRAS*, astro-ph/0905.4301
- Nolta M., et al., 2009, *ApJS*, 180, 296-305
- Oxley P., et al., 2004, *Proc. SPIE Int. Soc. Opt. Eng.*, 5543, 320-331, 2004
- Pascale E., 2008, et al., *ApJ*, 681, 400-414
- Piacentini F., et al., 2006, *ApJ*, 647, 833-839
- Polenta G., et al., 2005, *JCAP* 0511, 001
- Press, W. H., Flannery, B. P., Teukolsky, S. A. & Vetterling, W. T., *Numerical Recipes in FORTRAN, The Art of Scientific Computing*, 2nd Edition Cambridge University Press, Cambridge, 1992
- Samtleben D., et al., 2007, *Nuovo Cimento*, 122B, 1353-1358
- Sayers J., et al., 2009, *ApJ*, 690, 1597-1620
- Schultz, B., et al., in *Millimeter and Submillimeter Detectors and Instrumentation for Astronomy IV*. Edited by Duncan, William D.; Holland, Wayne S.; Withington, Stafford; Zmuidzinas, Jonas. *Proceedings of the SPIE*, Volume 7020, pp. 702022-702022-9 (2008)
- Siringo G., et al., *A&A*, 497, 945-962
- Swetz D.S., et al., 2008, *Proc. SPIE* 7020, 702008
- Verde, L., Wang, L., Heavens, A. F., & Kamionkowski, M., 2000, *MNRAS*, 313, 141
- Wilson G.W., et al., 2008, *MNRAS*, 385, 2225-2238
- Yoon K. W., et al., 2006, in *Millimeter and Submillimeter Detectors and Instrumentation for Astronomy III*, *Proceedings of SPIE*, 6275, astro-ph/0606278

Iteration	average (μK)	rms (μK)	skewness	kurtosis
no CR	0.0 ± 0.7	39.6 ± 0.4	-0.001 ± 0.038	0.022 ± 0.078
0 (R_1)	(1439 ± 6)	(159 ± 4)	(0.193 ± 0.070)	(0.06 ± 0.15)
1 (R_1)	(529 ± 3)	(92.3 ± 2.1)	(0.231 ± 0.070)	(0.11 ± 0.15)
2 (R_1)	(173.8 ± 1.5)	(59.1 ± 0.8)	(0.092 ± 0.042)	(0.059 ± 0.087)
3 (R_1)	(94.3 ± 1.1)	(56.0 ± 0.6)	(0.020 ± 0.038)	(0.029 ± 0.076)
4 (R_1)	(81.4 ± 1.1)	(57.4 ± 0.6)	(0.014 ± 0.038)	(0.029 ± 0.076)
5 (R_1)	(79.3 ± 1.1)	(57.9 ± 0.6)	(0.012 ± 0.038)	(0.029 ± 0.077)
0 (R_3)	(12.5 ± 0.7)	(41.9 ± 0.5)	(0.069 ± 0.039)	(0.089 ± 0.087)
1 (R_3)	(1.1 ± 0.7)	(40.6 ± 0.4)	(0.001 ± 0.037)	(0.029 ± 0.078)
2 (R_3)	(0.8 ± 0.7)	(40.9 ± 0.4)	(0.001 ± 0.037)	(0.029 ± 0.077)
3 (R_3)	(0.8 ± 0.7)	(41.0 ± 0.5)	(0.001 ± 0.037)	(0.029 ± 0.078)
4 (R_3)	(0.8 ± 0.7)	(41.0 ± 0.4)	(0.001 ± 0.037)	(0.029 ± 0.078)
5 (R_3)	(0.8 ± 0.7)	(41.0 ± 0.4)	(0.001 ± 0.037)	(0.029 ± 0.078)

Table 1. Parameters of the 1-point distribution of pixel temperature estimates, versus iteration of the pixel-based despiking, for cases R_1 and R_3 , (observations of small maps, same conditions as in fig. 6 and fig. 8). Iteration 0 refers to the values without despiking. The first line reports the noise only case (no CRs). The errors describe the dispersion of the results over 3000 simulations.